Computers and Geosciences 125 (2019) 109–114

Contents lists available at ScienceDirect

Computers and Geosciences

journal homepage: www.elsevier.com/locate/cageo

Research paper

Fast, accurate solutions for 3D strain volumes in a heterogeneous half space

Walter Landry[a,*,1], Sylvain Barbot[b,2]

[a] IPAC, Caltech, Pasadena, CA, 91125, USA
[b] University of Southern California, 3651 Trousdale Parkway, Los Angeles, CA, 90089, USA

ABSTRACT

Deformation in the Earth displays many degrees of localization. The mechanics of faulting can be well represented by slip on a 2D surface discretized in piecewise linear boundary elements. Distributed anelastic deformation associated with fluid flow, magma transfer, or viscoelastic relaxation can be approximated by anelastic strain discretized in 3D volume elements. The stress, traction, and displacement kernels for these elements form the basis of forward and inverse modeling of Earth's deformation during the seismic cycle, volcanic unrest or hydrologic change. While there are a number of techniques for computing these kernels for 2D fault surfaces, the techniques for 3D strain volumes are less developed. To improve the models of Earth's deformation, we extend previous work to numerically calculate these kernels for 3D strain volumes in a heterogeneous half space. The model provides high-precision displacement and stress for all these cases in a self-consistent manner. We exploit the adaptive multi-grid elastic solver implemented in the software Gamra (Landry and Barbot, 2016) to compute the deformation induced by boundary and volume elements with high numerical efficency. We demonstrate the correctness of the method with analytic tests. We illustrate the performance by computing a large-scale model of postseismic deformation for the 2015 Mw 7.8 Gorkha, Nepal earthquake with heterogeneous material properties. The open-source, freely available software can be useful for the calculation of elasto-static Green's functions for localized and distributed deformation in a heterogeneous Earth.

1. Introduction

Deformation of the Earth's lithosphere at time scales relevant to the earthquake cycle is accommodated both by slip along 2D fault surfaces as well as distributed strain in 3D volumes. For example, in the lower crust and mantle asthenosphere, distributed anelastic deformation is responsible for loading faults and accommodating transient strains (Masuti et al., 2016). The kinematics of crustal deformation can be inferred from geodetic or seismic data during the interseismic, coseismic, and postseismic phases of the earthquake cycle (McGuire and Segall, 2003; Murray and Segall, 2005; Bartlow et al., 2011; Barbot et al., 2013; Sathiakumar et al., 2017; Amey et al., 2018; Nocquet, 2018). The development of these techniques in the last few decades has led to an explosion of knowledge on fault behavior (Rogers and Dragert, 2003; Bakun et al., 2005; Bletery et al., 2014; Wallace et al., 2017; Araki et al., 2017).

These methods have recently been extended to incorporate the distributed deformation of large domains of the lithosphere (Tsang et al., 2016; Lambert and Barbot, 2016; Barbot et al., 2017; Moore et al., 2017; Qiu et al., 2018; Barbot, 2018b), such that it is now possible to build models of Earth's deformation that represent fault slip and distributed strain consistently using elasto-static Green's functions. Analytic solutions for rectangular and triangular dislocations (Chinnery, 1961; Chinnery, 1963; Savage and Hastie, 1966; Sato and Matsu'ura, 1974; Okada, 1985; Okada, 1992; Nikkhoo and Walter, 2015; Gimbutas et al., 2012; Meade, 2007; Jeyakumaran et al., 1992) and tetrahedral and cuboidal strain volumes (Tsang et al., 2016; Lambert and Barbot, 2016; Barbot et al., 2017; Barbot, 2018a,b) allow us to build kinematic and dynamic models of lithosphere deformation on curved fault surfaces with distributed, off-fault anelastic strain.

Unfortunately, all these solutions share an important caveat as they can not represent lateral variations of elastic properties. These lateral variations can be significant, such as in the case of deep sedimentary basins and their role in fault loading in the Los Angeles area (Rollins et al., 2018).

The goal of this paper is to describe a reliable numerical method for constructing displacement and stress Green's functions for strain volumes in a heteregeneous half-space. The method builds upon a three-dimensional, adaptive, multi-grid elasticity solver that allows numerically efficient calculation of displacement and stress kernels (Landry and Barbot, 2016). We describe the modeling approach and high precision tests of the implementation in Section 2. We demonstrate the relevance of the technique by modeling postseismic deformation from the 2015 Mw 7.8 Gorkha, Nepal earthquake in Section 3. The algorithms described in this paper are implemented in Gamra, a freely available tool for realistic earthquake modeling (see Computer code availability).

* Corresponding author.
E-mail addresses: wlandry@caltech.edu (W. Landry), sbarbot@usc.edu (S. Barbot).
[1] Present Address: Walter Burke Institute for Theoretical Physics, Caltech, Pasadena, CA 91125, USA.
[2] W. Landry: Methodology, Software, Visualization, and Writing of the paper. S. Barbot: Methodology, Software, and Writing of the paper.

https://doi.org/10.1016/j.cageo.2019.01.001
Received 11 November 2018; Accepted 2 January 2019
Available online 11 January 2019

2. Methods

2.1. Deformation on a staggered mesh

The deformation of Earth's rocks can be broadly categorized into elastic and anelastic deformation. In our treatment, we specify a strain (caused by anelastic deformation) and solve for the resulting elastic deformation in the half space (Andrews, 1978; Barbot and Fialko, 2010; Noda and Matsu'ura, 2010; Barbot, 2018b). The elastic problem is linear, so we can separately compute the elastic deformation caused by individual elements of strain. Then we can add up all of the separate solutions to find the total elastic deformation. This linearity also enables inverse models of deformation, where at-depth deformation is deduced from measured surface deformation. After computing the surface deformation caused by each of the individual elements of at-depth deformation, linearity turns the inversion problem into a tractable matrix minimization problem (McGuire and Segall, 2003; Murray and Segall, 2005; Bartlow et al., 2011; Barbot et al., 2013; Sathiakumar et al., 2017; Amey et al., 2018; Nocquet, 2018).

In a previous paper (Landry and Barbot, 2016), those input strain elements were only allowed to be jumps in displacement on 2D rectangular surfaces. That enabled efficient numerical calculations of displacement and stress kernels, resulting in fairly realistic models of earthquakes as patches of slip along an earthquake fault. This paper generalizes that treatment to gradients across 3D tetrahedral and cuboidal volumes. More complicated geometries can be obtained by linear superposition.

To solve this elastic problem, we start with the equation for linear elasticity

$$\sigma_{ji,j} + f_i = 0, \tag{1}$$

where σ_{ij} is the elastic part of the Cauchy stress and f_i is a forcing term. We use Einstein summation notation, where each index i, j, k is understood to stand for x, y, and z in turn, repeated indices are summed, and commas (,) denote derivatives. This assumption is thought to be valid for seismo-tectonic activity with infinitesimal strain (Fialko et al., 2001). The elastic properties of material in the Earth are well described by Lame's first parameter λ and the shear modulus μ (Shaw et al., 2015; Wang et al., 2016; Simmons et al., 2010; Bassin et al., 2000; Dziewoński and Anderson, 1981). This allows us to write the elastic stress in terms of the elastic displacement v_i as

$$\sigma_{ji}(\vec{v}) \equiv \mu(v_{i,j} + v_{j,i}) + \delta_{ij}\lambda v_{k,k}\,. \tag{2}$$

Input strains are introduced through the forcing terms f_i. These forcing terms are carefully constructed to modify the solution for the derivative of the displacement $v_{i,j}$ so that they match the input strain. The displacement across a fault can be a step function. Although the strain away from the fault is well behaved, the strain on the fault itself would be a delta function. This requires us to be especially careful to avoid numerical difficulties.

Since we are also interested in quasi-static deformation, we can follow a similar line of reasoning to look at the time derivative of stress $\partial\sigma_{ij}/\partial t$ in terms of the velocity of deformation $\partial v_i/\partial t$. This results in formulas with the same functional form as equations (1) and (2). Because a large breadth of physical processes can be captured within the same functional form, solving equations (1) and (2) with realistic material properties can find a broad range of applications (Tsang et al., 2016; Moore et al., 2017; Qiu et al., 2018; Barbot, 2018b).

The numerical method we use to solve these equations is largely described in a previous paper (Landry and Barbot, 2016). To summarize, we use a parallel multigrid solver on a staggered, adapted finite difference grid as in Fig. 1. To account for the input strain, we add carefully constructed forcing terms δf_i that depend on the mesh size. For example, when Eq. (1) is expanded out, it includes the term $(\mu v_{x,x})_{,x}$. Expressing this derivative at point $A = (A_x, A_y)$ in Fig. 1 using standard

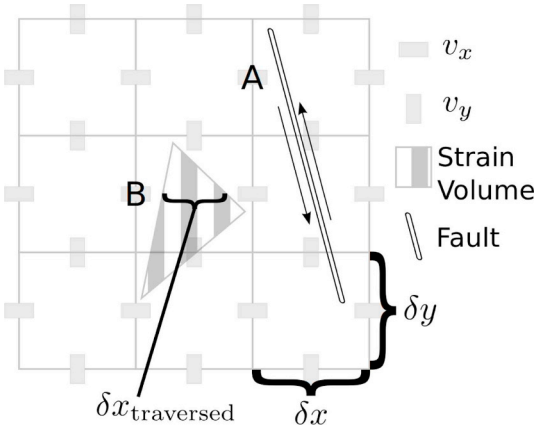

Fig. 1. Dislocations and strain volumes on a staggered grid. In 2D, dislocations are lines and strain volumes are triangles or rectangles. In 3D, the dislocations are triangles or rectangles, and strain volumes are either tetrahedra or cuboids. So this figure can represent either 2D grids or slices of 3D grids. The stencil for $(\mu v_{x,x})_{,x}$ at point A gives rise to a forcing term proportional to the slip s_x. At point B, the forcing term is proportional to $\varepsilon_{xx}\delta x_{\text{traversed}}$.

finite differences gives

$$(\mu v_{x,x})_{,x}|_{A_x,A_y} = \left[\mu|_{A_x+\delta x/2,A_y}\left(v_x|_{A_x+\delta x,A_y} - v_x|_{A_x,A_y}\right) - \mu|_{A_x-\delta x/2,A_y}\left(v_x|_{A_x,A_y} - v_x|_{A_x-\delta x,A_y}\right)\right]/\delta x^2, \tag{3}$$

where δx is the width of each finite difference cell and the notation $\mu|_{x,y}$ denotes the value of μ at the coordinate (x, y). For the fault near A, the fault creates a step function s_i in the solution for the displacement v_i. In this case, the appropriate forcing term at A for the $(\mu v_{x,x})_{,x}$ term turns

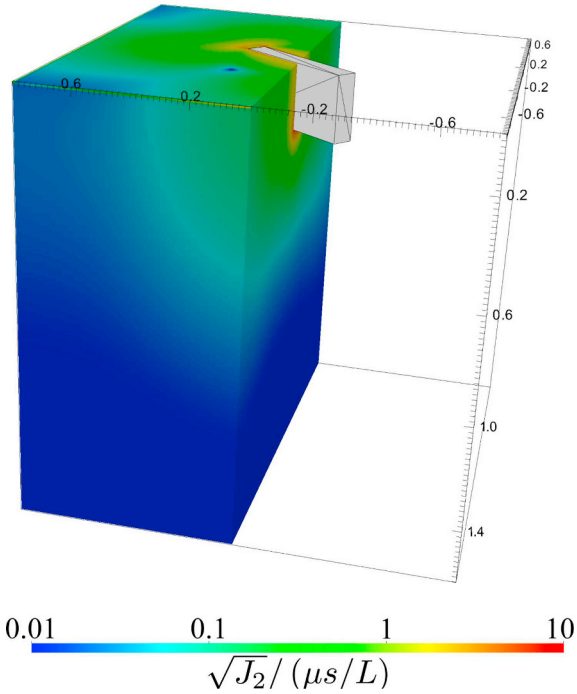

Fig. 2. A cutout of the invariant of the scaled deviatoric stress $J_2 = (\sigma_{ij}\sigma_{ji} - \sigma_{ii}\sigma_{jj}/3)/2$ of a computed solution for a single cuboidal strain volume. The equivalent resolution of the finest level is 256 × 256 × 256. The strain volume, indicated in grey, is made up of 6 tetrahedra and has dimensions $L = 0.50$, $W = 0.25$, $H = 0.08$. Each tetrahedra has shear strain components $\varepsilon_{LH} = \varepsilon_{HL} = 1600$, so the total slip across the narrow part of the block is $s = \varepsilon_{LH} \times H = 1600 \times 0.08 = 128$. The moduli are constant ($\mu = 1.6$, $\lambda = 1.5$). We set the boundary conditions (normal Dirichlet and shear stress) from the analytic solution in (Lambert and Barbot, 2016; Barbot et al., 2017).

Table 1
The ℓ_∞ norm of the error of v_x for a computed solution of a cuboid strain volume as a function of grid spacing h, where $\ell_\infty(\delta v_x) \equiv \max|(v_x)_{\text{computed}} - (v_x)_{\text{analytic}}|$. The strain volume has shear strain components $\varepsilon_{LH} = \varepsilon_{HL} = 1600$ and dimensions $L = 0.50$, $W = 0.25$, $H = 0.08$. The moduli are constant ($\mu = \lambda = 1$). We set the boundary conditions (normal Dirichlet and shear stress) from the analytic solution in (Lambert and Barbot, 2016; Barbot et al., 2017). The displacement is regular, so the convergence is uneven but monotonic.

h	$\ell_\infty(\delta v_x)$
0.1	26.54
0.05	3.191
0.025	1.545
0.0125	1.222
0.00625	0.4033

out to be

$$\delta f_x|_{A_x,A_y} = -s_x \mu|_{A_x+\delta x/2,A_y}/\delta x^2. \tag{4}$$

Since the displacement v_i is no longer continuous, we also have to take care when interpolating results for multigrid. After working through all of the details, described in (Landry and Barbot, 2016), the result is that the interpolation stencils acquire some extra constant terms.

2.2. 3D strain volumes

The main advance of this paper is the generalization of this framework to strain volumes. We consider tetrahedra or cuboids with a piecewise uniform anelastic strain ε_{ij}. A realistic distributed strain can be modeled by adding up many of these individual elements. This uniform strain corresponds to a gradient in the displacement. Consider Fig. 1. The computed difference in v_i between $(B_x + \delta x, B_y)$ and (B_x, B_y) depends on how much of the strain volume is traversed by the stencil. In this case, the difference for v_x is $\varepsilon_{xx}\delta x_{\text{traversed}}$. Using this, we compute a forcing term for strain volumes in a manner similar to that used to compute Eq. (4), giving

$$\delta f_x|_{B_x,B_y} = -\varepsilon_{xx}\delta x_{\text{traversed}}\, \mu|_{B_x+\frac{\delta x}{2},B_y}/\delta x^2. \tag{5}$$

Comparing this with Eq. (4), the only difference is replacing s_x with $\varepsilon_{xx}\delta x_{\text{traversed}}$. This means that after computing $\varepsilon_{ij}\delta x^j_{\text{traversed}}$ for all of the strain volumes, we can reuse all of the machinery for adaptive multigrid solutions that we previously employed for dislocations.

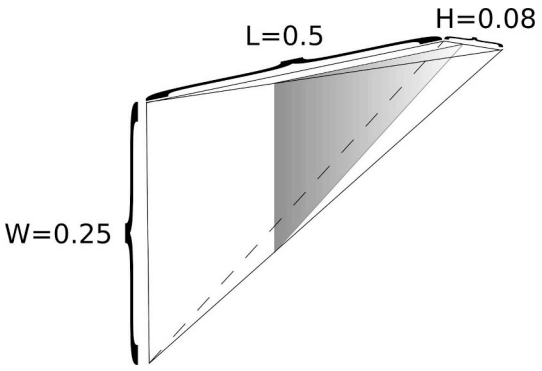

Fig. 3. Dimensions of the single tetrahedra used for testing variable moduli in strain volumes. To verify the implementation, we also approximate the strain volume with a large number of triangular faults distributed along the H axis. The shaded triangle is a representative single fault. So the triangular faults start out as big as the side of the tetrahedra and then converge to a single point.

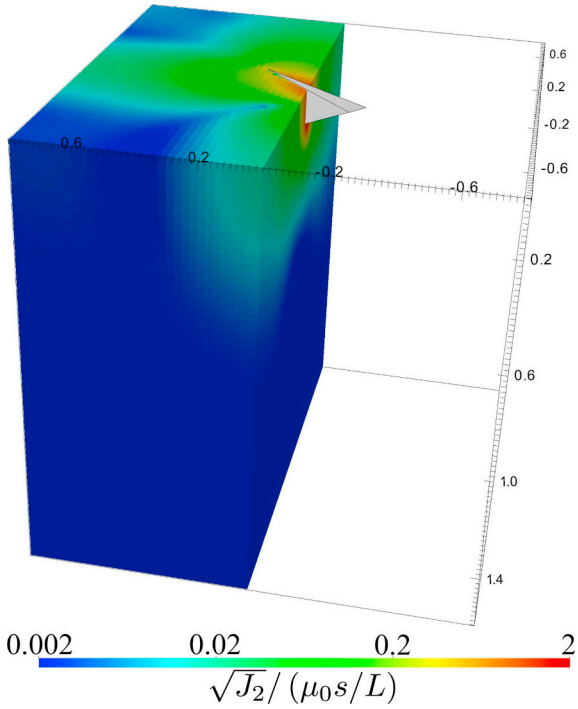

Fig. 4. A cutout of the invariant of the scaled deviatoric stress $J_2 = (\sigma_{ij}\sigma_{ji} - \sigma_{ii}\sigma_{jj}/3)/2$ of a computed solution for a single tetrahedral strain volume. The equivalent resolution of the finest level is $64 \times 64 \times 64$. The tetrahedra is the same as one of the tetrahedra making up the block in Fig. 2, and has a single non-zero shear strain component $\varepsilon_{LH} = 1600$. The moduli are not uniform, but set to $\mu = \mu_0 + 3x + 5y$, $\lambda = \lambda_0 - 2x + 7y$, where $\mu_0 = 10$ and $\lambda_0 = 10$. The boundary conditions are zero normal displacement and zero stress.

For testing our implementation, we start with the analytic solution for a cuboid aligned with the surface (Lambert and Barbot, 2016; Barbot et al., 2017). Fig. 2 shows the cuboid, constructed out of 6 tetrahedra, and the computed solution for this arrangement. Table 1 demonstrates the convergence of the ℓ_∞ error in v_x. We also implement cuboids directly, and the solutions are identical to the solutions of cuboids made up of tetrahedra.

To test more complicated volumes with variable moduli, we create a model using one of the tetrahedra from Fig. 2. Fig. 3 shows the dimensions of the tetrahedra, and Fig. 4 shows a solution for the stress. We do not have an analytic solution for this setup, but we can approximate a tetrahedral strain volume with a number of small triangular faults as in Fig. 3. This approach works very well at coarse resolution. At higher resolution, the mesh can resolve the spaces between the faults, so the details start to differ more significantly. Table 2 demonstrates that the two methods converge as the number of faults increases. This gives us some confidence in the correctness of our implementation of strain volumes with heterogeneous elasticity.

3. The 2015 Mw 7.8 Gorkha, Nepal earthquake

As an illustration of the relevance and performance of the proposed modeling approach, we model the initial post-seismic relaxation of the 2015 Mw 7.8 Gorkha, Nepal earthquake to incorporate hetergeneous material properties. This earthquake (Avouac et al., 2015; Galetzka et al., 2015; Elliott et al., 2016) took place on the Main Himalayan Front, a megathrust that separates the Indian and Eurasian plates (Tapponnier et al., 1986). The main shock was followed by a detectable transient deformation (Wang and Fialko, 2015; Gualandi et al., 2015) that was compatible with calculations of accelerated fault slip in the

Table 2
The ℓ_∞ norm of the difference in v_x between solutions that use a tetrahedral strain volume directly and one approximated with N small triangular faults. The setup is the same as in Fig. 4. The triangular faults are evenly distributed along the width ($H = 0.08$) as shown in Fig. 3. The slip on each triangular fault is $\varepsilon_{LH} \times H/N$.

N	$\ell_\infty(\delta v_x)$
128	0.4129
256	0.1645
512	0.0750
1024	0.0520

down-dip extension of the rupture and viscoelastic flow in the lower crust of Southern Tibet (Zhao et al., 2017). Our goal is to partially replicate these calculations by computing the instantaneous velocity induced by viscoelastic flow in the lower crust of the down-going plate. This calculation in the heterogeneous Earth has not been possible without constructing complicated meshes.

To do this, we first use Gamra to compute the stresses caused by the initial earthquake using the realistic slip model from (Qiu et al., 2016) (Fig. 5). We set the elastic moduli using the spherically symmetric 1D Preliminary Reference Earth Model (PREM) (Dziewoński and Anderson, 1981). Other than a straightforward extension of Gamra to handle triangular patches, this is an application of the algorithm described in a previous paper (Landry and Barbot, 2016).

This gives us a stress distribution throughout the bulk. This stress causes viscoelastic flow in the lower crust. We model the lower crust as a ramp, centered on the Main Himalayan Front, that dives from 20 to 40 km down to 50–70 km (Cattin and Avouac, 2000). We discretize this ramp using 2304 cuboids, each $15 \times 15 \times 5$ km. Dividing the computed stress by an assumed viscosity of 10^{20} Pa s gives us an instantaneous strain rate on each cuboid.

Using these strain rate cuboids as input, we use Gamra again, but this time computing the instantaneous strain rate in the bulk (Fig. 6). The solution encompasses a box $600 \times 600 \times 300$ km. The boundary conditions on the side and bottom are free slip: zero shear stress rate and zero normal velocity. The boundary conditions on the top are free surface: zero shear velocity and zero normal stress rate.

The adapted mesh ranges from a resolution of 9300 m down to 146 m. This is equivalent to a fixed resolution of $4096 \times 4096 \times 2048$. We set the refinement criteria to refine when the difference between solutions in the induced velocity at different levels of refinement error is greater than 10^{-11} cm/s. This is about 20 times smaller than the error due to the boundaries being only 300 km away. A uniform mesh would require about 3×10^{10} elements, but the adapted mesh only requires 6×10^7 elements.

In comparison with our previous work with faults made up of 2D surfaces, viscoelastic deformation occurs at a greater depth and is more distributed. The resulting strain rate is more diffuse, requiring relatively more mesh refinement over a larger volume. The viscoelastic model took 26 h to solve on a Dell R720 with 16 physical cores (Intel Xeon CPU ES-2670).

4. Conclusions and future work

We have demonstrated that we can robustly and accurately model arbitrary distributions of strain in tetrahedral and cuboidal volumes embedded in a hetergeneous half space. A particular advantage of the adaptive mesh is that computing the velocity field due to any single strain volume is faster than for the overall lower crust model, because the mesh can remain coarse far away from the source. This makes the approach well suited for the calculation of elasto-static Green's functions for localized (e.g., faulting) and distributed (e.g., viscoelastic) deformation.

While the approach is sufficient for a large class of problems, there are still some significant limitations. Topography can play a major influence on the surface displacements when there are large topographic gradients or if the deformation source is shallow (such as during volcanic unrest (Cayol and Cornet, 1998; Williams and Wadge, 2000) or underground explosions (Wang et al., 2018)). In addition, the effect of the Earth's curvature can play an important role for long-wavelength deformation (Pollitz, 1996). Also, coupling of deformation with the gravity field (Pollitz, 1996) is detectable for particularly large earthquakes (Han et al., 2006, 2014; Vallée et al., 2017). These areas will be the focus of future work.

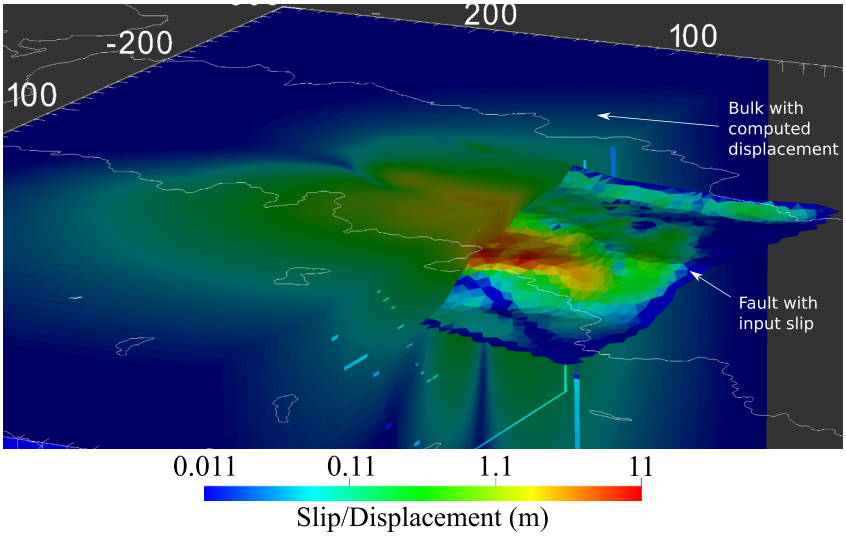

Fig. 5. A cutout of the input slip and computed displacement for the 2015 Mw 7.8 Gorkha, Nepal earthquake. The scale of the model is marked in km, and the political boundaries of Nepal are superimposed for reference.

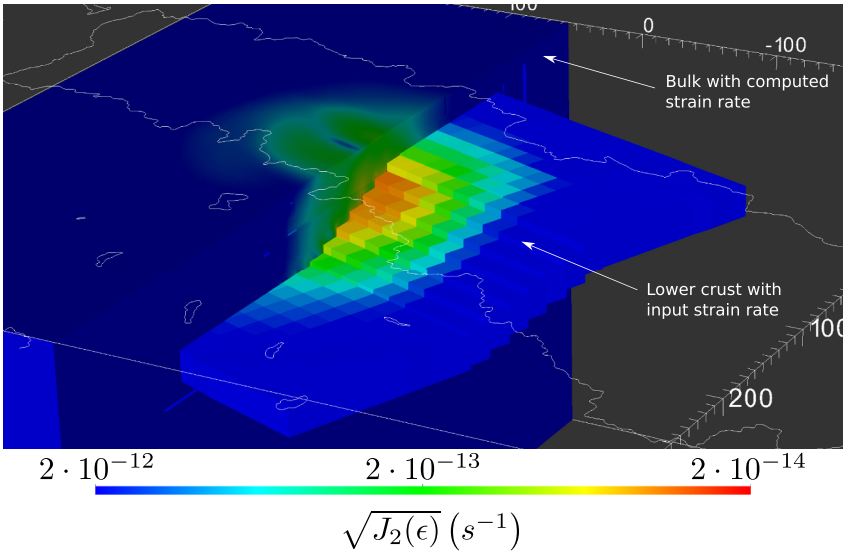

Fig. 6. A cutout of the input and computed instantaneous strain rates for the 2015 Mw 7.8 Gorkha, Nepal earthquake. We plot the second invariant of the symmetrized strain rate $J_2(\varepsilon) = (\varepsilon_{ij}\varepsilon_{ji} - \varepsilon_{ii}\varepsilon_{jj}/3)/2$. The scale of the model is marked in km, and the political boundaries of Nepal are superimposed for reference.

Acknowledgements

This research was supported by the National Research Foundation of Singapore under the NRF Fellowship scheme (National Research Fellow Award No. NRF-NRFF2013-04) and by the Earth Observatory of Singapore and the National Research Foundation and the Singapore Ministry of Education under the Research Centres of Excellence initiative.

Appendix A. Supplementary data

Supplementary data to this article can be found online at https://doi.org/10.1016/j.cageo.2019.01.001.

Computer code availability

The algorithms described in this paper are implemented in Gamra (Landry and Barbot, 2016), which is available at https://bitbucket.org/wlandry/gamra. Gamra is written in C++ , uses MPI for parallelism, and depends on a number of packages: HDF5 (The HDF Group, 2000–2010), SAMRAI (Hornung and Kohn, 2002; Hornung et al., 2006; The SAMRAI Team, 1997–2017), FTensor (Landry, 2003; Landry and Sacristan, 2001–2017), libokada (Landry, 2013–2017), muparser (Berg, 2014), and Boost (Boost Authors, 2003–2018). Gamra runs on everything from laptops to supercomputers. While Gamra is still under active development, the version associated with this paper has the Mercurial (The Mercurial Team, 2005–2018) changeset ID.

b2d412042fb39cf780ccce431bfb4f476ac74bd7.

References

Amey, R., Hooper, A., Walters, R., 2018. A Bayesian Method for Incorporating Self-Similarity Into Earthquake Slip Inversions. J. Geophys. Res 123 (7), 6052–6071.
Andrews, D., 1978. Coupling of energy between tectonic processes and earthquakes. J. Geophys. Res. 83 (B5), 2259–2264.
Araki, E., Saffer, D.M., Kopf, A.J., Wallace, L.M., Kimura, T., Machida, Y., Ide, S., Davis, E., Expedition, I., et al., 2017. Recurring and triggered slow-slip events near the trench at the Nankai Trough subduction megathrust. Science 356 (6343), 1157–1160.
Avouac, J.-P., Meng, L., Wei, S., Wang, T., Ampuero, J.-P., 2015. Lower edge of locked Main Himalayan Thrust unzipped by the 2015 Gorkha earthquake. Nat. Geosci. 8 (9), 708–711.
Bakun, W.H., Aagaard, B., Dost, B., Ellsworth, W.L., Hardebeck, J.L., Harris, R.A., Ji, C., Johnston, M.J.S., Langbein, J., Lienkaemper, J.J., Michael, A.J., Murray, J.R., Nadeau, R.M., Reasenberg, P.A., Reichle, M.S., Roeloffs, E.A., Shakal, A., Simpson, R.W., Waldhauser, F., 2005. Implications for prediction and hazard assessment from the 2004 Parkfield earthquake. Nature 437 (7061), 969–974.
Barbot, S., 2018a. Asthenosphere Flow Modulated by Megathrust Earthquake Cycles. Geophys. Res. Lett. 45 (12), 6018–6031. https://doi.org/10.1029/2018GL078197.
Barbot, S., 2018b. Deformation of a Half-Space from Anelastic Strain Confined in a Tetrahedral Volume. Bull. Seism. Soc. Am. 108 (5A) 2687. https://doi.org/10.1785/0120180058.
Barbot, S., Fialko, Y., 2010. A unified continuum representation of postseismic relaxation mechanisms: semi-analytic models of afterslip, poroelastic rebound and viscoelastic flow. Geophys. J. Int. 182 (3), 1124–1140. https://doi.org/10.1111/j.1365-246X.2010.04678.x.
Barbot, S., Agram, P., De Michele, M., 2013. Change of Apparent Segmentation of the San Andreas Fault Around Parkfield from Space Geodetic Observations Across Multiple periods. J. Geophys. Res. 118 (12), 6311–6327.
Barbot, S., Moore, J.D., Lambert, V., 2017. Displacement and Stress Associated with Distributed Anelastic Deformation in a Half-Space. Bull. Seism. Soc. Am. 107 (2), 821–855.
Bartlow, N.M., Miyazaki, S., Bradley, A.M., Segall, P., 2011. Space-time correlation of slip and tremor during the 2009 Cascadia slow slip event. Geophys. Res. Lett. 38 (18), 1–6.
Bassin, C., Laske, G., Masters, G., 2000. The Current Limits of Resolution for Surface Wave Tomography in North America. Eos 81, F897.
Berg, I., 2014. muparser - Fast Math Parser Library. http://muparser.beltoforion.de/.
Bletery, Q., Sladen, A., Delouis, B., Vallée, M., Nocquet, J.-M., Rolland, L., Jiang, J., 2014. A detailed source model for the Mw9.0 Tohoku-Oki earthquake reconciling geodesy, seismology, and tsunami records. J. Geophys. Res. 119 (10), 7636–7653.
Boost Authors, 2003-2018. Boost C++ Libraries. http://www.boost.org/.
Cattin, R., Avouac, J., 2000. Modeling mountain building and the seismic cycle in the Himalaya of Nepal. J. Geophys. Res. 105 (B6), 13389–13407.
Cayol, V., Cornet, F.H., 1998. Effects of topography on the interpretation of the deformation field of prominent volcanoes - Application to Etna. Geophys. Res. Lett. 25 (11), 1979–1982.
Chinnery, M., 1961. The deformation of the ground around surface faults. Bull. Seism. Soc. Am. 51 (3), 355–372.
Chinnery, M., 1963. The stress changes that accompany strike-slip faulting. Bull. Seism. Soc. Am. 53 (5), 921–932.
Dziewoński, A.M., Anderson, D.L., 1981. Preliminary reference Earth model. Phys. Earth Planet. In. 25 (4), 297–356.
Elliott, J., Jolivet, R., González, P., Avouac, J.-P., Hollingsworth, J., Searle, M., Stevens, V., 2016. Himalayan megathrust geometry and relation to topography revealed by the Gorkha earthquake. Nat. Geosci. 9 (2), 174–180.
Fialko, Y., Simons, M., Agnew, D., 2001. The complete (3-D) surface displacement field in the epicentral area of the 1999 M_w7.1 Hector Mine earthquake, southern California, from space geodetic observations. Geophys. Res. Lett. 28, 3063–3066.
Galetzka, J., Melgar, D., Genrich, J.F., Geng, J., Owen, S., Lindsey, E.O., Xu, X., Bock, Y., Avouac, J.-P., Adhikari, L.B., et al., 2015. Slip pulse and resonance of the Kathmandu basin during the 2015 Gorkha earthquake, Nepal. Science 349 (6252), 1091–1095.
Gimbutas, Z., Greengard, L., Barall, M., Tullis, T.E., 2012. On the Calculation of Displacement, Stress, and Strain Induced by Triangular Dislocations. Bull. Seismol. Soc. Am. 102 (6), 2776–2780.
Gualandi, A., Avouac, J.P., Galetzka, J., Genrich, J.F., Blewitt, G., Adhikari, L.B., Koirala, B.P., Gupta, R., Upreti, B.N., Pratt-Sitaula, B., et al., 2017. Pre- and post-seismic deformation related to the 2015, Mw 7.8 Gorkha earthquake, Nepal. Tectonophysics 714, 90–106.
Han, S.-C., Shum, C.K., Bevis, M., Ji, C., Kuo, C.-Y., 2006. Crustal Dilatation Observed by GRACE after the 2004 Sumatra-Andaman Earthquake. Science 313, 658–662. https://doi.org/10.1126/science.1128661.

Han, S.-C., Sauber, J., Pollitz, F., 2014. Broadscale postseismic gravity change following the 2011 Tohoku-Oki earthquake and implication for deformation by viscoelastic relaxation and afterslip. Geophys. Res. Lett. 41 (16), 5797–5805.
Hornung, R.D., Kohn, S.R., 2002. Managing application complexity in the SAMRAI object-oriented framework. Concurrency Comput. Pract. Ex. 14, 347–368.
Hornung, R.D., Wissink, A.M., Kohn, S.R., 2006. Managing complex data and geometry in parallel structured AMR applications. Eng. Comput 22, 181–195. http://doi:.org/10.1007/s00366-006-0038-6.
Jeyakumaran, M., Rudnicki, J., Keer, L., 1992. Modeling slip zones with triangular dislocation elements. Bull. Seismol. Soc. Am. 82 (5), 2153–2169.
Lambert, V., Barbot, S., 2016. Contribution of viscoelastic flow in earthquake cycles within the lithosphere-asthenosphere system. Geophys. Res. Lett. 43 (19), 142–154.
Landry, W., 2003. Implementing a High Performance Tensor Library. Sci. Program. 11, 273–290.
Landry, W., 2013-2017. Libokada: a library for analytic solutions of fault patches and strain volumes. https://bitbucket.org/wlandry/libokada.
Landry, W., Barbot, S., 2016. Gamra: Simple meshing for complex earthquakes. Comput. Geosci. 90, 49–63. https://doi.org/10.1016/j.cageo.2016.02.014.
Landry, W., Sacristan, M., 2001-2017. The FTensor library. https://bitbucket.org/wlandry/ftensor.
Masuti, S., Barbot, S.D., Karato, S.-i., Feng, L., Banerjee, P., 2016. Upper-mantle water stratification inferred from observations of the 2012 Indian Ocean earthquake. Nature 538 (7625), 373–377.
McGuire, J.J., Segall, P., 2003. Imaging of aseismic fault slip transients recorded by dense geodetic networks. Geophys. J. Int. 155 (3), 778–788.
Meade, B.J., 2007. Algorithms for the calculation of exact displacements, strains, and stresses for triangular dislocation elements in a uniform elastic half space. Comput. Geosci. 33 (8), 1064–1075.
Moore, J.D., Yu, H., Tang, C.-H., Wang, T., Barbot, S., Peng, D., Masuti, S., Dauwels, J., Hsu, Y.-J., Lambert, V., et al., 2017. Imaging the distribution of transient viscosity after the 2016 Mw 7.1 Kumamoto earthquake. Science 356 (6334), 163–167.
Murray, J., Segall, P., 2005. Spatiotemporal evolution of a transient slip event on the San Andreas fault near Parkfield, California. J. Geophys. Res. 110 (B9), 1–12.
Nikkhoo, M., Walter, T.R., 2015. Triangular dislocation: an analytical, artefact-free solution. Geophys. J. Int. 201 (2), 1117–1139.
Nocquet, J., 2018. Stochastic static fault slip inversion from geodetic data with non-negativity and bound constraints. Geophys. J. Int. 214 (1), 366–385.
Noda, A., Matsu'ura, M., 2010. Physics-based GPS data inversion to estimate three-dimensional elastic and inelastic strain fields. Geophys. J. Int. 182 (2), 513–530.
Okada, Y., 1985. Surface deformation due to shear and tensile faults in a half-space. Bull. Seismol. Soc. Am. 75 (4), 1135–1154.
Okada, Y., 1992. Internal deformation due to shear and tensile faults in a half-space. Bull. Seismol. Soc. Am. 82, 1018–1040.
Pollitz, F.F., 1996. Coseismic deformation from earthquake faulting on a layered spherical Earth. Geophys. J. Int. 125 (1), 1–14.
Qiu, Q., Hill, E.M., Barbot, S., Hubbard, J., Feng, W., Lindsey, E.O., Feng, L., Dai, K., Samsonov, S.V., Tapponnier, P., 2016. The mechanism of partial rupture of a locked megathrust: The role of fault morphology. Geology 44 (10), 875–878.
Qiu, Q., Moore, J.D., Barbot, S., Feng, L., Hill, E.M., 2018. Transient rheology of the Sumatran mantle wedge revealed by a decade of great earthquakes. Nat. commun 9 (1), 995.
Rogers, G., Dragert, H., 2003. Episodic tremor and slip on the Cascadia subduction zone: The chatter of silent slip. Science 300 (5627), 1942–1943.
Rollins, C., Avouac, J.P., Landry, W., Argus, D.F., Barbot, S., 2018. Interseismic strain accumulation on faults beneath Los Angeles, California. J. Geophys. Res 123 (8), 7126–7150. https://doi.org/10.1029/2017JB015387.
Sathiakumar, S., Barbot, S.D., Agram, P., 2017. Extending Resolution of Fault Slip With Geodetic Networks Through Optimal Network Design. J. Geophys. Res. 122 (12), 10,538–10,558. https://doi.org/10.1002/2017JB014326.
Sato, R., Matsu'ura, M., 1974. Strains and tilts on the surface of a semi-infinite medium. J. Phys. Earth 22 (2), 213–221.
Savage, J.C., Hastie, L.M., 1966. Surface deformation associated with dip-slip faulting. J. Geophys. Res. 71 (20), 4897–4904.
Shaw, J.H., Plesch, A., Tape, C., Suess, M.P., Jordan, T.H., Ely, G., Hauksson, E., Tromp, J., Tanimoto, T., Graves, R., et al., 2015. Unified structural representation of the southern California crust and upper mantle. Earth Planet. Sci. Lett. 415, 1–15.
Simmons, N.A., Forte, A.M., Boschi, L., Grand, S.P., 2010. GyPSuM: A joint tomographic model of mantle density and seismic wave speeds. J. Geophys. Res 115 (B12), 1–24.
Tapponnier, P., Peltzer, G., Armijo, R., 1986. On the mechanics of the collision between India and Asia. Geological Society, London, Special Publications 19 (1), 113–157.
The HDF Group, 2000-2010. Hierarchical data format version 5. http://www.hdfgroup.org/HDF5.
The Mercurial Team, 2005-2018. Mercurial source control management. https://www.mercurial-scm.org/.
The SAMRAI Team, 1997-2017. SAMRAI: structured adaptive mesh refinement application infrastructure. https://computation.llnl.gov/projects/samrai/applications.
Tsang, L.L., Hill, E.M., Barbot, S., Qiu, Q., Feng, L., Hermawan, I., Banerjee, P., Natawidjaja, D.H., 2016. Afterslip following the 2007 Mw 8.4 Bengkulu earthquake in Sumatra loaded the 2010 Mw 7.8 Mentawai tsunami earthquake rupture zone. J. Geophys. Res. 121 (12), 9034–9049.
Vallée, M., Ampuero, J.P., Juhel, K., Bernard, P., Montagner, J.-P., Barsuglia, M., 2017. Observations and modeling of the elastogravity signals preceding direct seismic waves. Science 358 (6367), 1164–1168.
Wallace, L.M., Kaneko, Y., Hreinsdóttir, S., Hamling, I., Peng, Z., Bartlow, N., D'Anastasio, E., Fry, B., 2017. Large-scale dynamic triggering of shallow slow slip enhanced by overlying sedimentary wedge. Nat. Geosci. 10 (10), 765.
Wang, K., Fialko, Y., 2017. Observations and Modeling of Coseismic and Postseismic Deformation Due To the 2015 Mw 7.8 Gorkha (Nepal) Earthquake. J. Geophys. Res. 123 (1), 761–779. https://doi.org/10.1002/2017JB014620.
Wang, M., Hubbard, J., Plesch, A., Shaw, J.H., Wang, L., 2016. Three-dimensional seismic velocity structure in the Sichuan basin, China. J. Geophys. Res. 121 (2), 1007–1022.
Wang, T., Shi, Q., Nikkhoo, M., Wei, S., Barbot, S., Dreger, D., Bürgmann, R., Motagh, M., Chen, Q.-F., 2018. The rise, collapse, and compaction of Mt. Mantap from the 3 September 2017 North Korean nuclear test. Science 361 (6398), 166–170. https://doi.org/10.1126/science.aar7230.
Williams, C.A., Wadge, G., 2000. An accurate and efficient method for including the effects of topography in three-dimensional elastic models of ground deformation with applications to radar interferometry. J. Geophys. Res. 105 (B4), 8103–8120.
Zhao, B., Bürgmann, R., Wang, D., Tan, K., Du, R., Zhang, R., 2017. Dominant Controls of Downdip Afterslip and Viscous Relaxation on the Postseismic Displacements Following the Mw7. 9 Gorkha, Nepal, Earthquake. J. Geophys. Res. 122 (10), 8376–8401.